

Hardware Software Co-Design Based Reconfigurable Radar Signal Processing Accelerator for Joint Radar-Communication System

Shragvi Sidharth Jha*, Aakanksha Tewari*, Sumit J Darak, Akanksha Sneh, Shobha Sundar Ram, *Senior Member IEEE*,

Abstract—Millimeter wave (mmW) codesigned 802.11ad-based joint radar communication (JRC) systems have been identified as a potential solution for realizing high bandwidth connected vehicles for next-generation intelligent transportation systems. The radar functionality within the JRC enables accurate detection and localization of mobile targets, which can significantly speed up the selection of the optimal high-directional narrow beam required for mmW communications between the base station and mobile target. To bring JRC to reality, a radar signal processing (RSP) accelerator, co-located with the wireless communication physical layer (PHY), on edge platforms is desired. In this work, we discuss the three-dimensional digital hardware RSP framework for 802.11ad-based JRC to detect the range, azimuth, and Doppler velocity of multiple targets. We present a novel efficient reconfigurable architecture for RSP on multi-processor system-on-chip (MPSoC) via hardware-software co-design, word-length optimization, and serial-parallel configurations. We demonstrate the functional correctness of the proposed fixed-point architecture and significant savings in resource utilization ($\sim 40-70\%$), execution time ($1.5\times$ improvement), and power consumption (50%) over floating-point architecture. The acceleration on hardware offers a 120-factor improvement in execution time over the benchmark Quad-core processor. The proposed architecture enables on-the-fly reconfigurability to support different azimuth precision and Doppler velocity resolution, offering a real-time trade-off between functional accuracy and detection time. We demonstrate end-to-end RSP on MPSoC with a user-friendly graphical user interface (GUI).

Index Terms—Algorithms to architecture, Hardware-software co-design, Joint radar communication, Multi-processor system-on-chip, Radar signal processing, Reconfigurability.

I. INTRODUCTION

Dual functional joint radar and communication waveforms, algorithms, and prototypes are being researched in response to spectral congestion issues. They can be broadly divided into research focusing on interference management between independently developed radar and communication systems [1–4]; opportunistic exploitation of radar transmission for secondary communication applications [4]; and vice versa [5–7]; and collaborative design of radar and communications functionalities using commonly shared waveform and hardware platform [8, 9]. The proposed work in this paper falls under this third category where we focus on a novel digital hardware prototype implementation of a radar signal processing (RSP) accelerator for a co-designed joint radar communication (JRC) system for millimeter wave (mmW) vehicular communications.

Over the last decade, vehicle-to-everything (V2X) communications is being researched for increased road safety and improved driver and passenger comfort for realizing semi and fully-autonomous driving. The state-of-the-art V2X communication protocols - such as the dedicated short-range communications [10], device-to-device based V2X [11] and cellular V2X [12] - operate at sub-6GHz carrier frequencies and hence do not support large bandwidths required for sharing time-critical high definition three-dimensional environmental sensing information. The alternative that has been suggested is high bandwidth mmW V2X communications supported by IEEE 802.11ad/ay protocols [13]. Interestingly, the preamble within the packet structure of these protocols has demonstrated perfect autocorrelation properties that make them attractive for radar remote sensing. Hence, there have been several recent works that have investigated the use of the IEEE 802.11ad protocol for JRC purposes. [6, 7, 14].

In general, there has been significant research focus on JRC waveform generation [23, 24] and algorithms [25, 26], but limited research on experimental demonstrations of JRC software/hardware prototypes. In [27], the architecture, design details, and software prototype of an IEEE802.11ad-based JRC transceiver were presented. In [22], the authors presented a hardware prototype on a universal software radio peripheral platform where they studied interference management between independently generated communication and radar waveforms. A codesigned JRC hardware prototype based on index modulation was presented in [19] where the transmitting antennas were divided into radar-centric and communication-centric subarrays. JRC transmission was experimentally demonstrated in [20] with separate radar and communications receivers. In [21], IEEE802.11ay access points were retrofitted for indoor radar detection of humans. In these works, the RF/mmW data are downconverted, digitized, and then processed offline in programming platforms (such as MATLAB, Python, etc.) through double-precision floating-point implementations.

For real-world deployments, the RSP must be realized on the edge platforms (for example, on wireless nodes mounted on road infrastructure, unmanned aerial vehicles, etc.), preferably with fixed point architecture. On such platforms, resource utilization, execution time, power consumption, and reconfigurability become critical design parameters that must be optimized. The mapping of algorithms on such platforms is essential to validate their feasibility on the hardware, and the availability of hardware IPs is an essential step toward commercialization. In this work, we focus specifically on the digital hardware implementation of the RSP component of the 802.11ad-based JRC receiver on the multi-processor system on chip (MPSoC) platform and consider multiple mobile target

*Shragvi Sidharth Jha and Aakanksha Tewari are joint first-authors.

All authors are with the Indraprastha Institute of Information Technology Delhi, New Delhi 110020 India. E-mail: {shragvi19207,aakankshat,sumit,shobha.akankshas}@iiitd.ac.in.

TABLE I: Literature survey comparing the contributions of the proposed work with the prior art

Reference	HSCD	RSP on Edge	Multiple Targets Detection	JRC Waveform	JRC Codesign	Reconfigurability	3D Localization
[15]	✓	✗	✗	✗	✗	✓	✗
[16]	✓	✗	✗	✗	✗	✓	✗
[17]	✓	✓	✓	✗	✗	✗	✓
[18]	✓	✓	✓	✗	✗	✗	✗
[19]	✗	✗	✓	✓	✗	✗	✗
[20]	✗	✓	✓	✓	✓	✗	✗
[21]	✗	✓	✓	✓	✓	✗	✗
[22]	✗	✗	✓	✓	✗	✗	✗
Proposed work	✓	✓	✓	✓	✓	✓	✓

detection and localization. The objective of the work is to provide the research community with reconfigurable hardware IPs obtained via mapping of the RSP algorithm on the MPSoC using hardware-software co-design (HSCD), and word-length (WL) optimization. We perform in-depth performance analysis and demonstrate complete functionality via a Graphical User Interface (GUI).

The field programmable gate array (FPGA) based MPSoC is one of the popular edge platforms which offers scalable architecture enabling a wide range of products using a common architecture. It also offers complete flexibility at software, interface, and hardware levels, thereby supporting in-field upgradation and feature richness. One such platform is Zynq MPSoC from AMD-Xilinx, comprising quad-core ARM processor as processing system (PS), i.e., software, and Ultrascale FPGA as programmable logic (PL), i.e., hardware¹ [28]. From a demonstration and analysis perspective, the MPSoC platform enables the mapping of algorithms entirely on PS or PL or partitioning between PS and PL via HSCD. In [15], HSCD of wireless transceivers for WLAN 802.11a protocol was developed on Zynq SoC; while [16] explored the HSCD of orthogonal frequency division modulation (OFDM) based *L*-band digital aeronautical communication system transceivers. In [17] OFDM-based pulse-modulated continuous wave radar prototype was implemented on Zynq MPSoC. In [18], the scattered radar signal corresponding to AC10 automotive radar [29] was processed on a Zynq SoC for localization of the target in terms of range and azimuth. The work presented in [30] explores deep learning-based wideband spectrum sensing on Zynq SoC.

The work presented in this paper deals with the design and implementation of three-dimensional RSP for an 802.11ad-based JRC system on the Zynq MPSoC platform. Based on our detailed literature review, limited works have been done in this direction. For easier understanding, we compare the existing works with the proposed work in terms of important design features and signal processing objectives in Table.I. The main contributions of the paper are summarized as follows:

- We model the complete radar transmitter with JRC waveform, wireless channels, radar target models, and radar receiver on the PS platform of the Zynq MPSoC using the PYNQ framework [31].
- We develop novel hardware IPs for RSP to estimate the range, azimuth, and Doppler velocity of multiple mobile targets. Each hardware IP has been optimized via WL optimization, serial-parallel architecture, and HSCD.
- We validate the functional correctness of each IP for a wide range of signal-to-noise ratios (SNR), and multiple

targets. We also demonstrate the gain in execution time due to FPGA-based acceleration.

- We integrate the complete RSP on Zynq MPSoC via HSCD and explore various configurations to lower execution time for given power and resource constraints.
- We demonstrate the on-the-fly reconfigurable nature of the proposed hardware architecture to support different azimuth resolutions, the number of packets, and Doppler velocity resolution.
- We develop a user-friendly GUI on the PYNQ platform to demonstrate the real-time performance of the proposed architectures.

Our paper is organized in the following manner. The following section presents the radar signal model and the RSP framework. In Section III, we present the mapping of the RSP algorithms to the hardware architecture on the MPSoC, followed by a detailed performance analysis including functional verification of range, Doppler, and azimuth estimation in single and multiple target scenarios in IV. We present a complexity analysis in Section V followed by a discussion on the reconfigurability in Section VI. Finally, we summarize the main scientific insights in Section VII.

Notation: Vectors and matrices are denoted with boldface lower and upper case characters respectively, while variables are denoted with regular characters. Vector superscript T denotes the transpose operation while the symbol $*$ denotes the complex conjugate transpose operation. Time domain and frequency domain representations of a vector are \mathbf{x} and $\tilde{\mathbf{x}}$ respectively. We use the square braces, $[\cdot]$, to indicate discrete-time sequences, and the curly braces, (\cdot) , to indicate continuous time signals. The symbols \mathbb{B} , \mathbb{R} , and \mathbb{C} are used to represent binary, real, and complex data, respectively.

II. JRC SYSTEM MODEL AND RSP FRAMEWORK

In this section, we detail the radar signal models and corresponding RSP functionalities that will be mapped into hardware as per the architectural framework proposed in [27] and recapitulated here. We consider a JRC base station, as shown in Fig.1, where the 802.11ad-based integrated radar/communication waveform is generated at the transmitter and is radiated through an omnidirectional beam from a single antenna of an antenna array. A Q element uniform linear array (ULA) is used in the BS receiver (BS-RX), where, each antenna element is connected to a distinct mmW chain (amplifier, demodulator, and analog-to-digital converter). Then radar scattered data from multiple mobile users/targets are gathered across the multiple receiver channels and are processed through digital beamforming to support their detection and localization. Subsequent communication between the base station and mobile target will be through high-directional narrow beams realized through analog

¹In this manuscript, PL, FPGA, and hardware are used interchangeably from hereon. Similarly, PS, ARM processor, and software are used interchangeably.

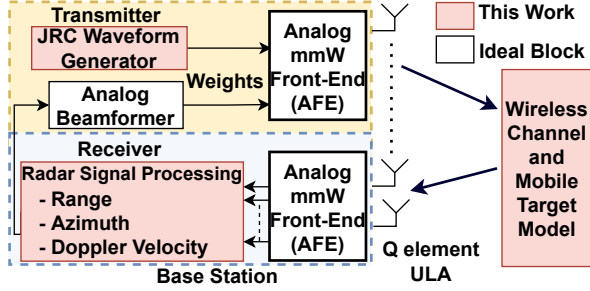


Fig. 1: Architecture overview of the JRC transceiver at the BS.

beamforming directed at the azimuth determined by the RSP. Note that in this work, we focus on the *digital baseband radar functionality* shown in the figure which includes the waveform generation at the transmitter and the RSP at the receiver. Hence, we do not discuss the analog/mmW front end or the communication framework in this manuscript.

A. Signal Model

As noted in prior work [6], the preamble of each n^{th} IEEE 802.11ad PHY frame consists of K -length Golay sequences, $\mathbf{g}_n \in \mathbb{B}^{K \times 1}$, that have perfect autocorrelation properties (zero sidelobes) to enable range estimation of remote targets. When the order of N Golay sequences is carefully chosen as per the recommendations of [7, 14], the resulting two-dimensional signal $\mathbf{G} = [\mathbf{g}_1, \dots, \mathbf{g}_N]$ is useful for range and Doppler estimation. When this digital signal is converted to analog, the resulting analog transmitted signal is

$$s_{tx}(t) = \sum_{k=0}^{K-1} \mathbf{G}[k, n] \delta(t - kT_s - nT_{PRI}), \quad (1)$$

where T_s is the sampling time for each bit in \mathbf{g}_n and T_{PRI} is the interval between two consecutive transmissions. Note that the duty cycle of the waveform KT_s/T_{PRI} is quite low since the Golay sequences in the preamble form a small section within the entire packet. Second, the optional training fields in the packet that are usually included for mmW beam training are omitted since beam selection is being carried out through radar. The duration of the entire signal is one coherent processing interval comprising NT_{PRI} . The signal is then suitably convolved with a transmit shaping filter, up-converted to mmW wavelength, λ , and radiated through the transmitting omnidirectional antenna. Assume that there are P targets within the radar field of view such that each p^{th} target is located at a range r_p , azimuth ϕ_p and moving with radial velocity v_p with respect to the radar. Then radar echoes from all P targets superpose on the Q element ULA of the receiver. Each q^{th} antenna element is supported by a corresponding RF/mmW processing chain comprising a low noise amplifier, inphase-quadrature demodulator, filter, and analog-to-digital converter. Hence, the received signal at the radar receiver, after downconversion and digitization, is a three-dimensional data cube, $\mathbf{S}_{rx} \in \mathbb{C}^{K \times Q \times N}$, across fast time (k), slow time (n) and antenna element (q) given by

$$\begin{aligned} \mathbf{S}_{rx} &= [\mathbf{S}_{rx_1}, \dots, \mathbf{S}_{rx_N}] \\ &= \sum_{p=1}^P a_p \mathbf{G}[n, k - k_p] e^{-j2\pi f_{D_p} n T_{PRI}} e^{j\frac{2\pi}{\lambda} d(q-1) \sin \phi_p} + \zeta. \end{aligned} \quad (2)$$

Here, a_p is the strength of each p^{th} target's returns which incorporates the two-way path loss factor between the

transmitting and receiving antenna and the radar cross-section; k_p is the sample index corresponding to the range-induced delay across fast time data; f_{D_p} is the velocity-induced Doppler shift across the slow time data, and $(q-1)d \sin \phi_p$ is the path delay to each q^{th} antenna element. Note that the range-azimuth data for each n^{th} packet is a two-dimensional data $\mathbf{S}_{rx_n} \in \mathbb{C}^{K \times Q}$. In the above model, we have assumed that the strength and the velocity of the mobile target are constant within the coherent time interval.

B. Radar Signal Processing (RSP) Framework for JRC

The radar data cube is processed in the following manner. We first process the radar data square, \mathbf{S}_{rx_n} , across each n^{th} packet to obtain the range-azimuth image. For this, we carry out matched filtering (MF) across the fast-time domain and Fourier-based digital beamforming across the multi-channel antenna data. Due to the computational complexity of carrying out cross-correlation across the fast time domain, we implement the MF through matrix multiplication in the frequency domain and subsequently inverse Fourier transform the results back to the time domain. Then we process the radar detections from this image across N packets to estimate the Doppler velocity as shown in Fig.2. The steps are as follows:

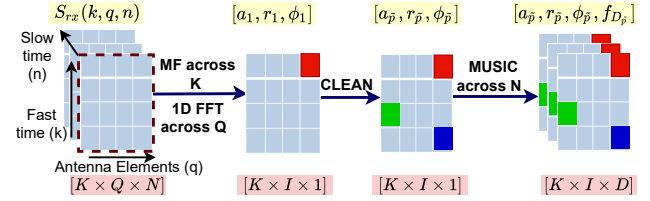


Fig. 2: Radar signal processing of three-dimensional radar data: matched filtering (in frequency domain) across fast time domain for range, FFT across antennas for azimuth, and MUSIC across slow time samples for Doppler estimation respectively.

Step.1. One Dimensional Fast Fourier Transform (1D-FFT) on K sample fast time data: We FFT each n^{th} transmitted Golay sequence to frequency domain (k_f): $\tilde{\mathbf{g}}_n[k_f] = \text{1D-FFT}\{\mathbf{g}_n[k]\}$. Note that this step can be carried out offline (since the transmit sequence is known ahead of real-time operation) in order to reduce real-time computational complexity. Similarly, we FFT the fast time data corresponding to each q^{th} receiver channel from the n^{th} packet: $\tilde{\mathbf{S}}_{rx_n}[k_f, q] = \text{1D-FFT}\{\mathbf{S}_{rx_n}[k, q]\}$, this time in real time.

Step.2. Digital Beamforming across Q channel data: Then, we generate $\Gamma_n \in \mathbb{C}^{K \times I}$ for every $\phi_i, i = 1 \dots I$ spanning the radar search space through azimuth increments of $\Delta\phi$, using the operation,

$$\tilde{\Gamma}_n[\phi_i] = \text{diag} \left[\tilde{\mathbf{S}}_{rx_n} \mathbf{w}_{\phi_i} \tilde{\mathbf{g}}_n^* \right]. \quad (3)$$

Here $\mathbf{w}_{\phi_i} = [1 \ e^{-jk_c d \sin \phi_i} \dots e^{-j(Q-1)k_c d \sin \phi_i}]^T$ provides a digital weight vector to the ULA receiver data to scan the beam at ϕ_i ; and diag extracts the diagonal elements of the complex $K \times K$ matrix generated by the matrix multiplication in equation (3).

Step.3. Inverse FFT (IFFT) across K frequency domain data: Then the frequency domain data for every ϕ_i in $\tilde{\Gamma}_n[\phi_i]$ is converted back to fast time domain through the IFFT: $\Gamma_n[r_k, \phi_i] = \text{IFFT}\{\tilde{\Gamma}_n[k_f, \phi_i]\}$. Note that the fast time domain

directly corresponds to the radar range domain (r_k) which is also of K samples with a range resolution of $\Delta r = \frac{cT_s}{2}$ and spans from 0 to $\frac{c(KT_s)}{2}$ where c represents the speed of light. Hence Γ_n provides a range-azimuth image of the target space corresponding to every n^{th} slow time sample/packet.

Step.4. CLEAN on Range-Azimuth radar images: Since the radar search space across range and azimuth may consist of several targets, of different scattering strengths, the sidelobes from the point spread response of one target may suppress weaker targets, thereby preventing their detection. Hence, we next implement the *CLEAN* algorithm to detect multiple targets [32, 33] as shown in equations (4) and (5). First, we initialize a two-dimensional matrix χ_1 to be equal to the range-azimuth space of the first packet (Γ_1). Then for each p^{th} iteration of the algorithm we identify the peak amplitude ($\hat{a}_{\bar{p}}$), and corresponding range ($\hat{r}_{\bar{p}}$) and azimuth ($\hat{\phi}_{\bar{p}}$) coordinates of the strongest/most dominant target scatterer in the radar search space as shown in equation (4). Then we obtain the residue, $\chi_{\bar{p}+1}$, for the subsequent iteration by removing the contributions of p^{th} target from the total response through equation (5).

$$\hat{a}_{\bar{p}} = \max \chi_{\bar{p}}, \hat{r}_{\bar{p}}, \hat{\phi}_{\bar{p}} = \arg \max_{r_k, \phi_i} \chi_{\bar{p}-1} \quad (4)$$

$$\chi_{\bar{p}+1} = \chi_{\bar{p}} - \hat{a}_{\bar{p}} \mathbf{h}(\hat{r}_{\bar{p}}, \hat{\phi}_{\bar{p}}) \quad (5)$$

In (5), $\mathbf{h}(\cdot)$ denotes the two-dimensional range-azimuth point spread response of a target located at the specified coordinates within the parentheses. The above steps are repeated up to a predetermined number \tilde{P} or while the overall strength of the residues is above a specified threshold. Note that \tilde{P} is a predetermined number that may be lesser, equal, or greater than the actual number of targets (P) which is not known. Second, this algorithm is only applied to the radar data from the first packet. For the subsequent packets, this step is skipped and we proceed directly to Step.5.

Step.5. Multiple signal classification (MUSIC) across slow time: Finally, once \tilde{P} targets are identified in the range-azimuth space, we estimate their Doppler through the application of MUSIC, a super-resolution algorithm [34], across the slow time domain for every $[\hat{r}_{\bar{p}}, \hat{\phi}_{\bar{p}}]$ cell as shown in Fig.2. Essentially, MUSIC is an algorithm that detects signal components by separating the signal from white noise subspace. First, we vectorize the data across the N slow time packets for each p^{th} target through $\mathbf{y}_{\bar{p}} = [\Gamma_1[\hat{r}_{\bar{p}}, \hat{\phi}_{\bar{p}}], \dots, \Gamma_N[\hat{r}_{\bar{p}}, \hat{\phi}_{\bar{p}}]]$. Then, we perform the eigenvector decomposition (EVD) of the auto-covariance matrix $\mathbf{Y}_{\bar{p}}$ by QR-decomposition method [35] as shown in

$$\mathbf{Y}_{\bar{p}} = \mathbf{y}_{\bar{p}} \mathbf{y}_{\bar{p}}^* = \mathbf{Q}_{\bar{p}} \mathbf{R}_{\bar{p}}. \quad (6)$$

Here, $\mathbf{R}_{\bar{p}} \in \mathbb{C}^{N \times N}$ converges to an upper triangle matrix and $\mathbf{Q}_{\bar{p}} \in \mathbb{C}^{N \times N}$ is an orthogonal matrix which comprise of the $\epsilon_{\bar{p}} \in \mathbb{C}^{N \times 1}$ and $\mathbf{E}_{\bar{p}} \in \mathbb{C}^{N \times N-1}$ that correspond to the signal and noise subspaces respectively. Then, the MUSIC spectrum is generated from

$$\mu_{\bar{p}}[f_D] = \frac{1}{v^*[f_D] \mathbf{E}_{\bar{p}} \mathbf{E}_{\bar{p}}^* v[f_D]} \quad (7)$$

where, $v[f_D]$ is the pseudo-Doppler delay axis for the Doppler frequency $f_D \in \mathbb{R}^{1 \times D}$ spanning from $-f_{D_{max}}$ to $f_{D_{max}}$ with a resolution of Δf_D . The Doppler $\hat{f}_{D_{\bar{p}}}$ corresponding to each p^{th} target is estimated from the coordinate of the peak of $\mu_{\bar{p}}$ ($\arg \max_{f_D} \mu_{\bar{p}}$).

Thus, at the end of the exercise, we obtain the estimates of the amplitude ($\hat{a}_{\bar{p}}$), range ($\hat{r}_{\bar{p}}$), azimuth ($\hat{\phi}_{\bar{p}}$) and Doppler frequency ($\hat{f}_{D_{\bar{p}}}$) of each p^{th} detected target with the precision of $\Delta r, \Delta \phi$ and Δf_D . The Doppler information is subsequently used by the JRC to distinguish mobile users from static clutter; the range information is used to cluster multiple returns from a single extended target; while the azimuth information is used by the analog beamformer within the JRC transmitter for establishing directional communication links with the mobile users. This process is out of the scope of this work and hence not discussed any further in this manuscript.

III. RECONFIGURABLE RSP ARCHITECTURE

This section discusses the mapping of the RSP algorithms for the estimation of range, azimuth and Doppler velocity of multiple targets discussed in the previous section on the proposed reconfigurable architecture realized on PL. At the end of the section, we present the complete integrated architecture and demonstration via a suitable GUI.

A. 1D-FFT

The first signal processing task in the proposed RSP architecture is to perform the 1D-FFT on the K samples received from each of the Q antennas, $\mathbf{S}_{rx_n} \in \mathbb{C}^{K \times Q}$, (Step.1. in the Section II-B). This operation will have to take place in real time since it operates upon the received radar data. As shown in Fig. 3, the complex IQ demodulated samples received from each RF/mmW chain are buffered in the block RAM (BRAM) of the FPGA (A) using the direct memory access (DMA). We use separate BRAM for real and imaginary components of the received data.

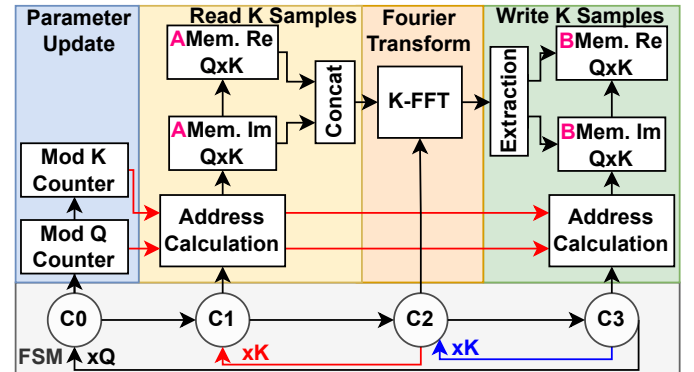


Fig. 3: One-dimensional FFT on K samples of data from each q^{th} antenna from n^{th} packet.

Then, the FFT of size K is performed using the IP provided by AMD-Xilinx, and the output is stored in another BRAM (B). The data movements between FFT IP, BRAMs A and B are controlled using the finite state machine (FSM) depicted in Fig. 3. Alternatively, we could simultaneously perform the FFT operation across multiple antennas by using multiple FFT IPs in a serial-parallel fashion to reduce execution time. Since each BRAM has a limited number of read and write ports, we would also need to partition the BRAMs, in this strategy, so that the data for multiple FFTs can be read and written simultaneously.

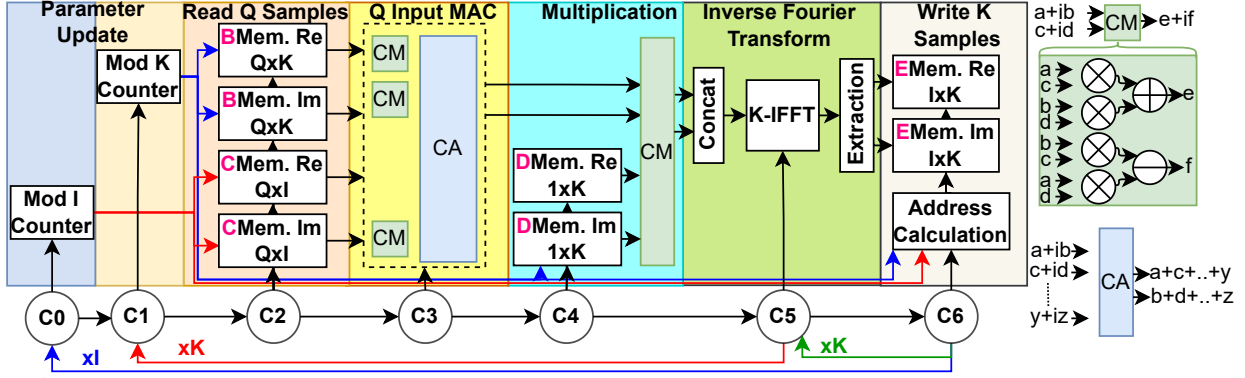


Fig. 4: Digital beamforming and Inverse Fourier Transform architecture to estimate range and azimuth of a single target.

B. Digital Beamforming and Inverse FFT

After 1D-FFT on a single received packet, we have $Q \times K$ complex samples in BRAM B. **Step.2.** in the RSP block involves multiple (I) large-size matrix multiplication operations in equation (3) followed by the extraction of diagonal elements. The direct hardware realization of these operations is computationally complex. Hence, we exploit the significant redundancy associated with: (1) the selection of diagonal elements to obtain $\Gamma_n \in \mathbb{C}^{K \times I}$; and (2) the Q replicas of the \mathbf{g}_n , to realize a computationally efficient architecture implementation of equation (3) followed by the corresponding IFFT in **Step.3.** as shown in Fig. 4.

The matrix, $\mathbf{W} \in \mathbb{C}^{I \times Q}$, comprising of digital weight vector for all Q antennas and I azimuth values, is fixed. Hence, it is precomputed and initialized in BRAM C. In real-time, the first step is to perform element-wise complex multiplications (CM) between each column of BRAM B containing 1D-FFT output and the i^{th} column of BRAM C. These operations are performed using parallel Q CMs. Resultant Q outputs are accumulated using Q -input complex adder (CA) to obtain a single complex sample, which is multiplied with the corresponding sample of the precomputed frequency domain version of the transmitted Golay sequence ($\tilde{\mathbf{g}}_n[k_f], k_f = 1 \dots K$) stored in BRAM D. This process is repeated for each i^{th} column of BRAM B, as shown in the figure, to obtain K complex samples for a given azimuth, ϕ_i . Next, we perform the 1D-IFFT on K samples using AMD-Xilinx IP. This process is repeated for I azimuth values to obtain $I \times K$ samples in BRAM E.

The direct mapping of equation (3) incurs QK CMs for digital beamforming followed by K^2Q CM and $K^2(Q-1)$ -input CA. The proposed computationally efficient architecture also needs QK CMs for digital beamforming. However, it needs only KQ CMs and $K(Q-1)$ -input CA. Thus, the proposed architecture needs K times fewer CMs and CAs, offering significant savings in resource utilization, execution time, and power consumption. The BRAM memory requirement is also reduced by a factor Q due to the shifting of CA operations before the element-wise multiplication with the frequency domain version of the transmitted Golay sequence.

The proposed low-complexity architecture allows further parallelization to improve the execution time. For instance, the digital beamforming and 1D-IFFT are done sequentially I times, one for each azimuth value. Since the computations for any two azimuth values are independent, we have explored the serial-parallel configurations of the architecture in Fig. 4. Specifically, we have used multiple units of CMs,

CAs, and IFFT along with the BRAM partitions to allow simultaneous read and write operations. The FSM takes care of appropriate scheduling and movement of data across the parallel blocks. Please refer to Section V for more details about the performance gain using our architecture.

C. Range and Azimuth Estimation

The peak search algorithm in **Step.4. CLEAN operation** then uses the 1D-IFFT output to estimate the amplitude, range, and azimuth of the detected target. Since parallelization of this operation would demand complete partitions of memory, we implement a sequential execution of this operation in the PS section of the MPSoC. To summarize, whenever the new packet is received, the architectures in Fig. 3 and Fig. 4 are used by the scheduler in the PS to perform the data-intensive FFT, beamforming, and IFFT operations in the FPGA. We refer to this entire operation as MF. The PS reads the data from BRAM E via DMA and performs the peak search.

D. Multiple Packets Processing

The Doppler velocity estimation requires multiple packets received over the antenna sequentially. Each packet is processed by the architectures in Fig. 3 and Fig. 4 to obtain the $I \times K$ matrix. The peak selection unit in the PS selects one cell from each $I \times K$ matrix based on the estimated range and azimuth. These N samples extracted from N packets are processed by the MUSIC architecture in Section III-E to estimate the Doppler velocity of the detected target. After the first packet processing, the rest of the packets can be processed in parallel by using multiple instances of the architectures in Fig. 3 and Fig. 4.

E. MUSIC Based Doppler Velocity Estimation

The MUSIC algorithm, in **Step.5** of the RSP, comprises broadly three tasks: autocorrelation, EVD, and MUSIC spectrum generation (MSG). The input vector, $\mathbf{y}_{\bar{p}}$, is formed by selecting the values in the \bar{p}^{th} target's range-azimuth cell of $n = 1 : N$ packets after MF. Then, the vector is sent to the MUSIC accelerator in PL from PS through DMA. Figure 5 indicates that $\mathbf{y}_{\bar{p}}$ is read from BRAMs F and G and undergoes one-dimensional autocorrelation. The autocorrelation block is realized as separate complex conjugate multiplications for real and imaginary parts between each element of $\mathbf{y}_{\bar{p}}$, read from BRAM F and $\mathbf{y}_{\bar{p}}^*$ read from BRAM G. This is followed by a concatenation of real and imaginary parts to form the resultant $N \times N$ covariance matrix $\mathbf{Y}_{\bar{p}}$. As shown in the figure,

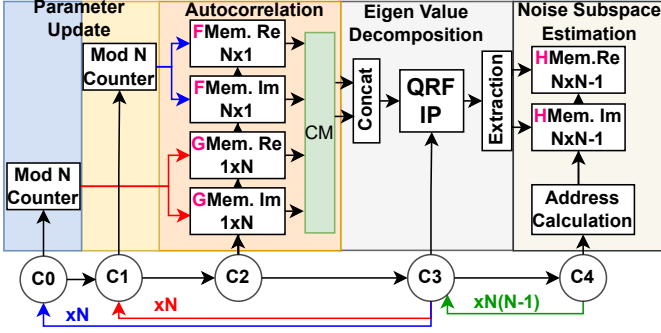


Fig. 5: Architecture corresponding to autocorrelation and EVD stages in MUSIC.

multiple CM units and the partitioning of the BRAM enable the parallelization of operations in the autocorrelation stage. Subsequently, EVD is performed on $\mathbf{Y}_{\bar{p}}$ via QR factorization method with the inbuilt AMD Xilinx QRF IP, wherein the matrix is iteratively decomposed into $\mathbf{Y}_{\bar{p}} = \mathbf{Q}_{\bar{p}}\mathbf{R}_{\bar{p}}$, until $\mathbf{R}_{\bar{p}}$ converges to an upper triangular matrix. The diagonal elements of the resultant $\mathbf{R}_{\bar{p}}$ are the eigenvalues arranged in descending order whereas $\mathbf{Q}_{\bar{p}}$ is an orthogonal matrix of the respective eigenvectors. $\mathbf{Q}_{\bar{p}}$ is partitioned into signal and noise subspaces. Since we are computing the Doppler of only a single target (at a specified range and azimuth), the signal subspace, $\epsilon_{\bar{p}}$, comprising a single eigenvector corresponding to the largest eigenvalue, is discarded, and the noise subspace $\mathbf{E}_{\bar{p}}$ with remaining $N - 1$ eigenvectors is further processed.

Fig. 6 illustrates the MSG as per equation (7). The Doppler matrix, $\mathbf{f}_D \in \mathbb{C}^{N \times D}$, is pre-computed and stored in BRAM I . In the beginning, element-wise multiplication and accumulation (MAC) are done for a given Doppler element and $(N - 1)$ eigenvectors. The output of MAC is squared and accumulated. As shown in the figure, N MAC operations for a given eigenvector are done in parallel but the computations for each $N - 1$ eigenvector are done sequentially. This process is repeated for D Doppler elements to obtain the $1 \times D$ size MUSIC spectrum. The peak search unit finds the maximum value to obtain the Doppler velocity of the detected target. The MUSIC spectrum is further normalized and converted to decibels for visualization.

F. Complete RSP Architecture for Multiple Target Detection Using Multiple Packets on MPSoC

The complete RSP architecture to detect multiple targets and estimate their peak amplitude, range, azimuth, and Doppler velocity on ZCU11 MPSoC from AMD-Xilinx is shown in Fig. 7. We have deployed PYNQ OS on the quad-core A53 processor in PS which handles hardware and peripheral initialization, communication with hardware drivers, and IPs. In addition, we have deployed some of the RSP tasks on PS. From the RSP perspective, the first task is to generate the transmit data packet as per the 802.11ad protocol as discussed in Section II-A. We have developed a user-friendly GUI, shown on the left side of the same figure, to allow users to select the number of targets, target parameters, SNR, and architecture for RSP. Then we generate the received baseband packets for Q antennas using wireless channel and radar target modeling in PS. The *Receiver Scheduler* process handles these tasks which are realized in the PS.

The next task is to detect the strongest target and estimate its parameters. The *Multiple Target Packet Scheduler* processes in PS sequentially, and sends all received packets to the MF block in PL via DMA. Depending on the available resources, the proposed architecture allows the parallel processing of multiple packets using parallel MF blocks and multi-channel DMAs as shown in the figure. Using the MF output of the first packet, the peak search process in PS calculates the range and azimuth of the first detected target. For performance analysis, root mean square error (RMSE) is calculated (as discussed in the later sections) and displayed on the GUI. Based on the MF outputs of all packets, the peak selection block selects the desired samples from the MF output and forms the packet for the MUSIC block in FPGA. This packet is sent to the MUSIC via DMA and the corresponding Doppler velocity is estimated. Then the FPGA transfers the complete MUSIC spectra for displaying on the GUI. The CLEAN algorithm implemented in PS is used to detect multiple mobile targets in the JRC field-of-view by utilizing the parameter information obtained from the previously localized target. The detected amplitude, range, and azimuth of the dominant target in each iteration are used to generate the point spread response ($\mathbf{h}(\cdot)$) as discussed in equation (5) for the subsequent target detection.

The *Multiple Target Packet Scheduler* processes in PS generates a dummy radar data cube signal corresponding to the dominant target in the most recent iteration and processes it using the MF in FPGA to generate the point spread response, which is then subtracted from the original response to obtain the residue for the next iteration. This process is followed by Doppler velocity estimation of the targets using MUSIC.

The proposed architecture is carefully designed to offer reconfiguration capability which enables the run-time selection of parameters such as the angular precision ($\Delta\phi$) for the azimuth radiation pattern, the number of packets (N), and Doppler elements (D) utilized for Doppler estimation. As shown in Fig. 4, we can configure the hardware IP to support different $\Delta\phi$ by adjusting the MOD I counter resolution. The PS does this via the AXI Lite port in the proposed architecture. Similarly, the number of packets in a coherent interval and Doppler elements can be easily controlled by controlling the number of times the DMA is configured since there is one DMA transaction per packet for MF IP. The MUSIC IP is configured for a given packet size and Doppler elements via the AXI Lite port in the proposed architecture. The impact of the reconfigurable architecture on execution time and power consumption are discussed later in Section VI.

IV. PERFORMANCE ANALYSIS

In this section, we validate the functional correctness of the proposed hardware architectures for different WL, SNR, and number of targets. We use, the root mean square error (RMSE) between the estimated range/azimuth/Doppler (denoted as \hat{x}) and their ground truth counterpart values (denoted as x) as shown in

$$RMSE = \sqrt{\frac{\sum_{n=1}^N (x - \hat{x})^2}{N}}, \quad (8)$$

as the performance metric. In our work, we have considered a total of $Q = 32$ antennas and $N = 100$ packets/slow time samples, each consisting of $K = 1024$ fast time samples generated by zero padding a Doppler-resilient Golay sequence of 512 bits. The radar field-of-view spans from 0 to 40 m along the range with $\Delta r = 0.085$ m; azimuth spans from -90° to

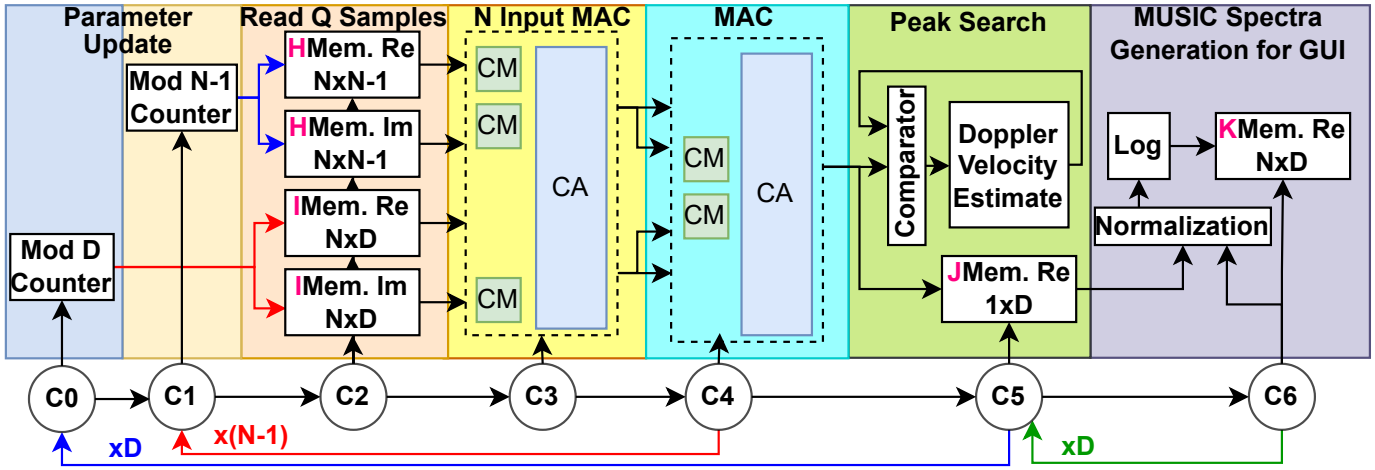


Fig. 6: Architecture corresponding to MUSIC spectrum generation stage.

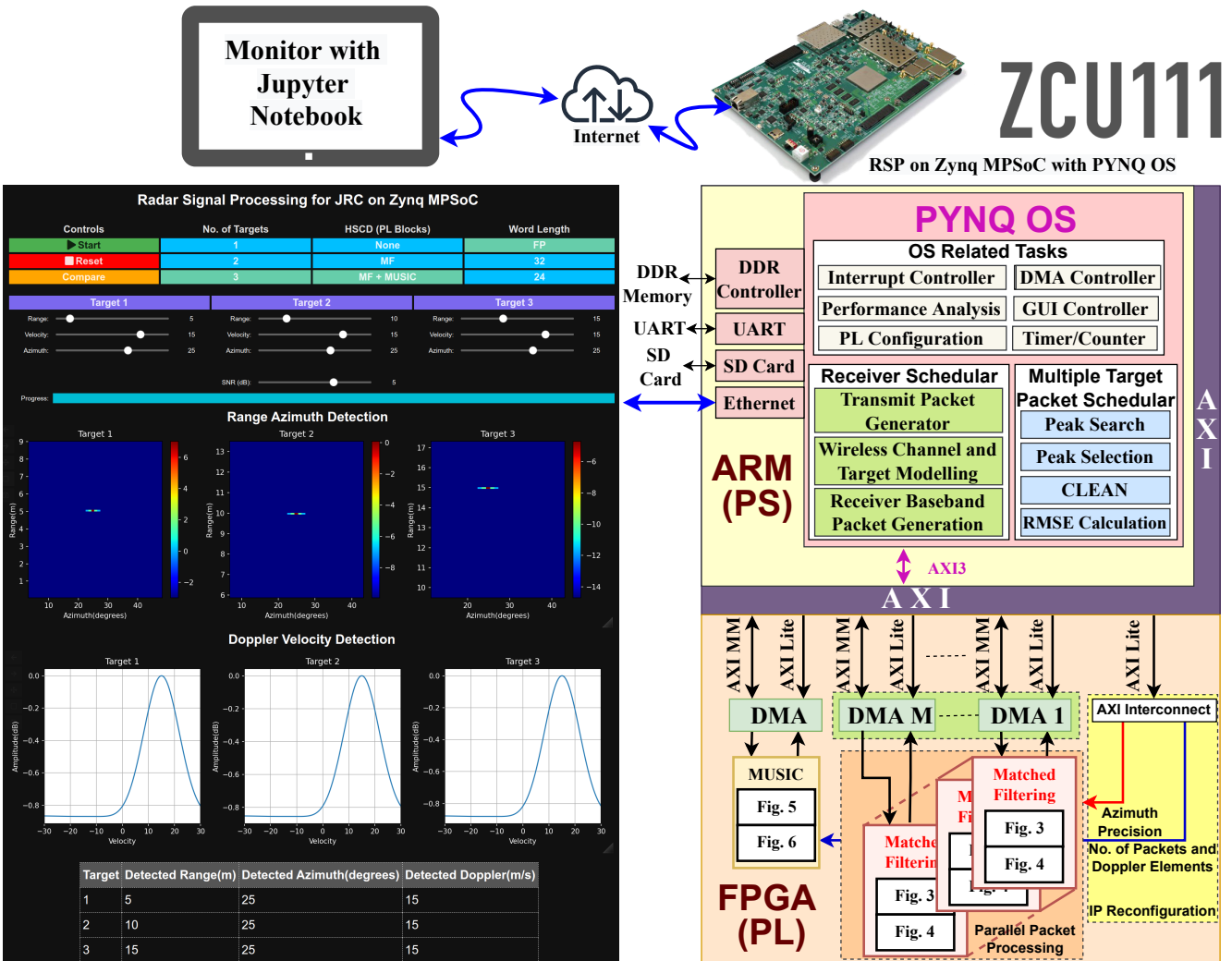


Fig. 7: Architecture overview of RSP implementation on Zynq MPSoC along with GUI. Here, Zynq MPSoC is connected to institute network and GUI is remotely accessible on any desktop or mobile phone with internet connectivity.

90° at $\Delta\phi = 1^\circ$; and the Doppler velocity spans -30 m/s to $+30$ m/s with a velocity resolution of 0.3 m/s. All the results presented hereafter are obtained after averaging over 200 different experiments. In each experiment, we consider

a three-target scenario where each target is treated as a point target whose position is a random vector uniformly distributed in the radar's field of view. The radar cross-section of each target is also a random variable and follows the Swerling-1

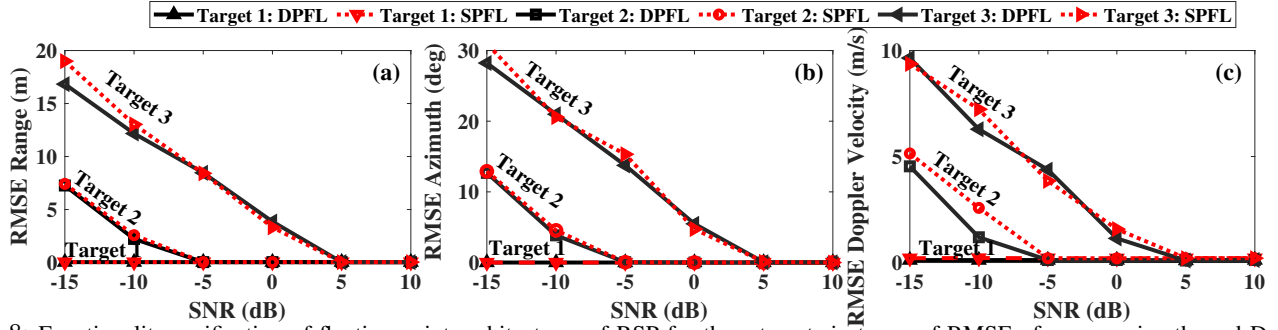


Fig. 8: Functionality verification of floating point architectures of RSP for three targets in terms of RMSE of range, azimuth, and Doppler velocity estimations.

(exponential) probability distribution which is most common for radar targets [36]. The average strengths of the first, second, and third targets are 10, 5, and 3 square meters, respectively. We consider a wide range of SNR from -15 dB to 10 dB to verify the functional correctness of fixed-point hardware IPs. In practice, the SNR range is expected to be 0 dB or higher.

A. Floating Point Architecture

In Fig. 8(a), we benchmark the range detection performance of the single precision floating point (SPFL) WL on the MPSoC with the double precision floating point (DPFL) WL in PS or MATLAB. The RMSE of both the MPSoC and MATLAB approaches is nearly identical for all targets and SNRs, validating the functional correctness of the proposed hardware architectures for range estimation. The results show that the RMSE is well below 0.5% for the first (or strongest) target for all SNRs. The RMSE degrades for the second and third targets. However, even here, the RMSE improves with the increase in SNR as expected. The poorer performance for the weaker targets is due to two reasons: First, the third detected target is likely to have a lower peak amplitude compared to the second detected target which will have a lower amplitude than the first target due to the nature of the algorithm; Second, due to the superposition of the returns from multiple targets, the CLEAN algorithm can never fully remove the contributions of the dominant scatterer in equation (5). This will result in error propagation across the iterations of the algorithm. The degradation becomes significant at low SNR. Numerically, the RMSE is lower than 0.5% for SNR higher than -5dB and 5 dB for the second and third targets, respectively. In Fig. 8(b), we compare the azimuth detection performance of both approaches. We observe similar behavior for SNR and multiple targets. In both cases, we have used a single packet to estimate the range and azimuth of all targets. Next, we compare the RMSE in Doppler velocity estimation in Fig. 8(c). There is no difference between the two approaches validating the functional correctness of the complete RSP architecture, including iterative CLEAN algorithm, peak search, point spread response generation, and MUSIC realized on the MPSoC.

B. Fixed-Point Architecture

We analyze the effect of WL on the functional correctness of the proposed hardware IPs. Ideally, the WL should be as small as possible, and fixed-point WL architectures are preferred over SPFL architectures due to lower resource utilization, execution time, and power consumption. We denote

the fixed-point WL as $\langle W, L \rangle$ where W is the total number of bits, and L and $W - L$ are the number of bits used to represent the integer and fractional parts of the real number respectively. To identify the desired WL, we first use a sufficiently large number value for W and vary the integer bits, L . This gives the minimum value L needed to represent all numerical values accurately. As shown in Fig. 9 (a), (b), and (c), a total of 5 integer bits are sufficient to ensure that the RMSE of range estimation for all three targets is the same as that of the SPFL implementation. The results are averaged over SNRs ranging from -15 to 10 dB.

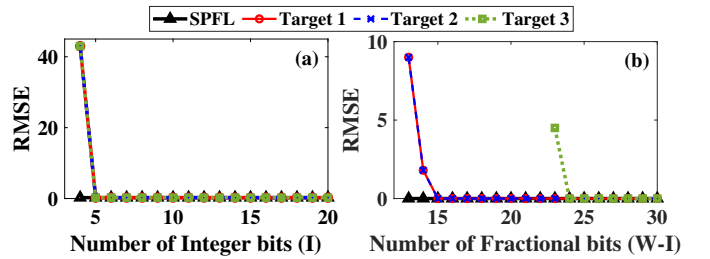


Fig. 9: Average range and azimuth RMSE of 3 targets for different WL: (a) RMSE vs. number of integer bits, I , for 30 fractional bits, (b) RMSE vs. number of fractional bits for 5 integer bits.

Next, we fix the number of integer bits to 5 and varied the W to identify the minimum number of bits, $(W - L)$, needed to represent fractional numbers accurately. As shown in Fig. 9 (d), (e), and (f), the value of $(W - L)$ is not the same for all the targets. The third target needs more bits than the first two targets. This is expected due to the lower amplitude of the third target and the error propagation across iterations in CLEAN as discussed earlier. Since we use the same IP for detecting all three targets, we use the WL of $\langle 24, 5 \rangle$ for MF IP. In the case of FFT and IFFT, we have used the IPs provided by AMD-Xilinx, which are optimized for SPFL WL.

Next, we verify the functional correctness of the fixed-point hardware MF IPs for a wide range of SNR for the range and azimuth estimation of the first, second, and third targets. As shown in Fig. 10 and Fig. 11, the selected WL of $\langle 24, 5 \rangle$ offers nearly the same RMSE as that of the SPFL architectures for all SNR under different target scenarios. Further reduction in WL to $\langle 19, 5 \rangle$ results in significant degradation in performance. The WL of $\langle 32, 5 \rangle$ has the same number of bits as that of SPFL, and both offer nearly identical RMSE. As discussed later, the former WL of $\langle 32, 5 \rangle$ and $\langle 24, 5 \rangle$ offer significant savings in resources, validating the importance of WL optimization on hardware.

For MUSIC-based Doppler estimation, the matrix arithmetic

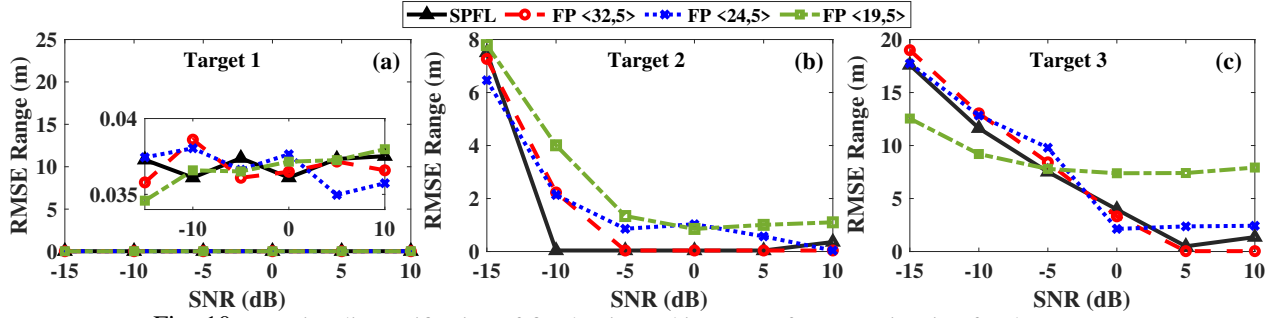


Fig. 10: Functionality verification of fixed point architectures of range estimation for three targets.

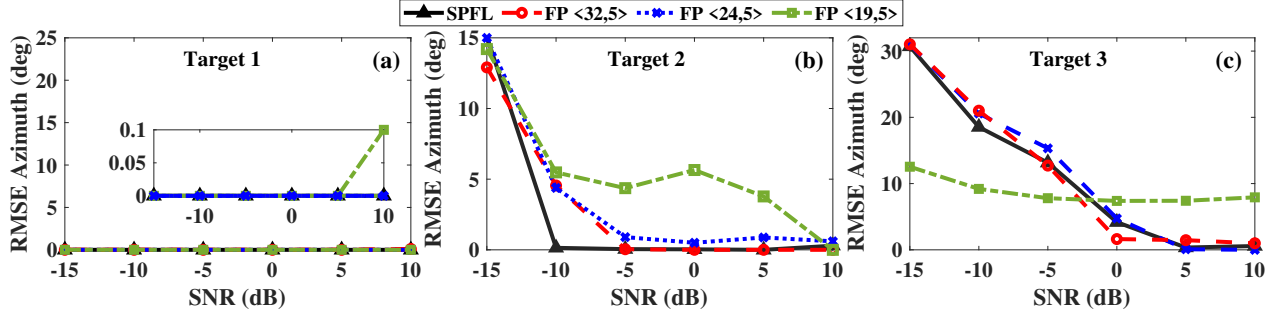


Fig. 11: Functionality verification of fixed point architectures of azimuth estimation for three targets.

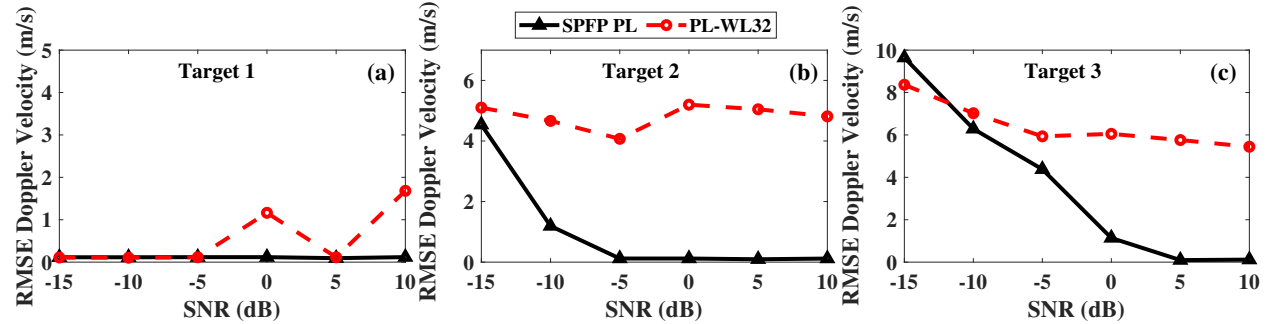


Fig. 12: Functionality verification of fixed point architectures of Doppler velocity estimation for three targets.

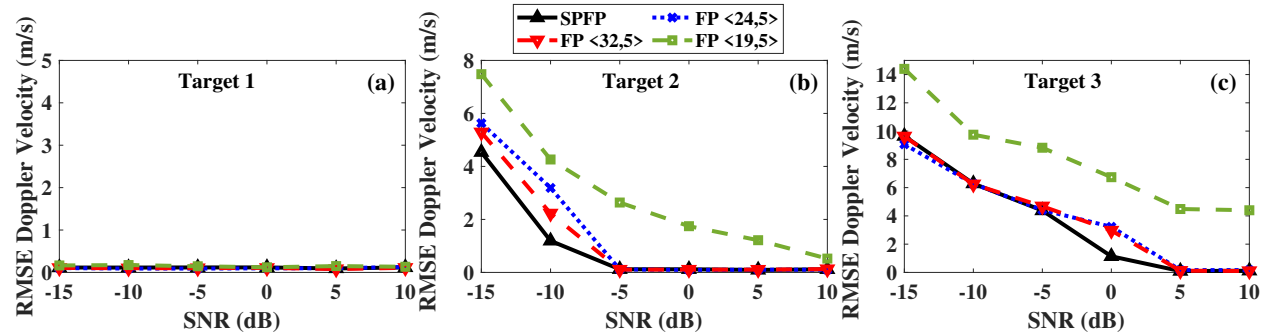


Fig. 13: Functionality verification of SPFL architecture of Doppler velocity estimation for different fixed-point MF architectures.

involving EVD demands a large dynamic range; hence, the fixed-point architecture incurs large RMSE. Using the SPFL MF IP, we analyze the RMSE in the Doppler velocity estimation using MUSIC IPs of different WL. As shown in Fig. 12, the performance degrades significantly for the fixed-point architecture of the MUSIC and hence, SPFL WL is preferred for Doppler velocity estimation. Since MUSIC-based Doppler velocity estimation depends on the MF IP output, we compare the performance of SPFL MUSIC IP for different

fixed-point architectures of MF IP. As shown in Fig. 13, the WL of $\langle 24, 5 \rangle$ does not affect the performance of Doppler velocity estimation, thereby validating the selected WL of $\langle 24, 5 \rangle$.

V. COMPLEXITY COMPARISON

This section compares the resource utilization, power consumption, and execution time of various architectures obtained via WL and HSCD optimizations. In Table II, we

TABLE II: Comparison of resource utilization and power consumption for different WLs

No.	Range and Azimuth Estimation WL	Doppler Velocity Estimation WL	BRAM		DSP		Flip Flops		Look Up Tables (LUTs)		Power	
			Utilization	Savings	Utilization	Savings	Utilization	Savings	Utilization	Savings	Consumption	Savings
1	SPFL	SPFL	1073	NA	1655	NA	144001	NA	151712	NA	6.59	NA
2	<32, 5>		818	24%	1163	30%	41001	71%	63382	58%	3.7	44%
3	<24, 5>		638	40%	600	64%	35078	76%	44152	71%	3.3	50%
4	<19, 5>		438	59%	374	77%	37924	74%	36481	76%	3.1	53%

compare the proposed architecture’s FPGA resource utilization and power consumption for four different WLs. It can be observed that the SPFL architecture consumes the highest amount of block RAM (BRAM), embedded DSP multiplier units, flip-flops (FFS), and FPGA look-up tables (LUTs). The dynamic power consumption of the SPFL architecture is the highest. The proposed architecture with WL of <32, 5> offers identical functional performance as that of SPFL architecture but significantly reduces resource utilization and power consumption. Further reduction of around 40-76% in resource utilization is achieved using the WL of <24, 5> without compromising functional accuracy for all three target detection as shown in the table. In the case of two target detection, we can further reduce the WL up to <19, 5> to gain 59-76% savings in resources and 53% in power consumption with a slight degradation in functional accuracy.

The HSCD divides the various tasks between PL/hardware (i.e., FPGA) and PS/software (i.e., ARM Processor). When algorithms are mapped on the FPGA, there are the benefits of reduced execution time for data-intensive computations and reconfigurability at the cost of increased power consumption and computational resources. We compare the time required to estimate the range and azimuth of the single target using one packet and the Doppler velocity of the single target using 100 packets. We assume all the packets are available in memory, so there is no time overhead for data communications between the PS and PL. As shown in Table III, the FPGA-based implementation results in a huge improvement in execution time with accelerator factors of 204 and 14.5 for range-azimuth and Doppler velocity estimation, respectively.

TABLE III: Comparison of execution time for RSP with SPFL WL

Target Parameter	Packets	Execution Time (Seconds)		Acceleration Factor
		PS	PS+PL	
Range and Azimuth	1	5.3	0.026	204
Doppler Velocity	100	1.1	0.077	14.5

Next, we consider the HSCD of the end-to-end RSP, which includes the transmitter, wireless channel, and target modeling followed by sequential reception and processing of 100 packets at the receiver using the proposed RSP architecture. As shown in Table IV, we compare the performance of various configurations with the configuration in Row 1, where complete processing is done in PS. Such a configuration does not require the FPGA; hence, the resource utilization is mentioned as not applicable (NA). However, this configuration incurs the highest execution time due to the sequential nature of the software processing; hence, the acceleration factor is mentioned as 1. Note that this is despite using an ARM Cortex A53 quad-core processor operating at 1.2 GHz compared to 300 MHz in FPGA. In addition, we have deployed the PYNQ operating system on PS, which runs the various algorithms on Python, allowing parallelism using multiple cores. The PS is also equipped with the Kali GPU operating at 600 MHz. Hence the Numpy-based implementation in Python can take advantage of these resources to reduce the execution time.

In all the configurations discussed next, CLEAN and peak search algorithms are realized in PS. In the second configuration (Row 2), we have moved the MUSIC-based Doppler velocity estimation to PL, which only slightly improved the execution time with an acceleration factor of 1.01. However, there is a significant increase in FPGA resource utilization and power consumption. In the third configuration (Row 3), we have moved the MF and FFT-based range and azimuth estimation in PL. The rest of the processing, including Doppler velocity estimation, is realized in PS. This configuration offers a significant acceleration factor of 76 over the first configuration. Similarly, in the fourth configuration (Row 4), all estimation algorithms are realized in PL, resulting in an acceleration factor of 104.

Though the third and fourth configurations offer good acceleration, they incur high resource utilization and power consumption. This can be reduced significantly by using fixed-point architectures, as shown in Rows 5 and 6 of Table IV. Further improvement in acceleration factor and reduction in resource utilization is possible by exploring fixed-point realization of the MUSIC. However, it is challenging due to the large number of packets that demand autocorrelation and EVD of high dimension signal. This demands more efforts towards the fixed-point realization of MUSIC for 3D RSP especially for large N .

In the existing architecture, the precision of azimuth estimation ($\Delta\phi$) is 1° , meaning there are 181 candidate angles when the search space is from -90° to $+90^\circ$. For each angle, we need to perform the MF operation in equation (3). Due to resource constraints, we can not have a fully parallel architecture with 181 MF IPs. In this direction, we explore a new configuration of the proposed architecture by having two MF IPs resulting in the serial-parallel configuration as shown in Row 7 of Table IV. As expected, a significant gain in acceleration factor is achieved with a slight increase in resource utilization and power consumption. Similar architecture can be explored for FFT operations which are currently being done sequentially by using single IP shared across all antennas. When we compare architectures in Rows 4 and 7, the architecture in Row 7 offers a 1.5 times higher acceleration factor, needs fewer resources and consumes less power. This validates the importance of careful HSCD, WL optimization, and serial-parallel architectures.

VI. RECONFIGURABLE ARCHITECTURE

This section discusses the reconfigurable architectures that offer an on-the-fly (real time) switching between hardware configurations and trade-offs between functional accuracy, execution time, and power consumption.

In the previous sections, we assumed $\Delta\phi$ to be 1° and $|I| = 181$ (for ϕ_i spanning -90° to $+90^\circ$). In many application scenarios, we may however need lower precision in the beginning and finer precision later. For instance, base stations may need to identify clusters of users quickly using a coarse sectoral search before estimating the accurate azimuth of each user in a given cluster. The proposed

TABLE IV: Comparison of acceleration factor, resource utilization and power consumption for different HSCD configurations

No.	Blocks in PL	WL	Acceleration Factor	BRAM	DSP	Flip Flops	LUTs	Dynamic Power (W)
1	NA	SPFL	1	NA				XX
2	Doppler Velocity	SPFL	1.01	262	350	28923	40800	3.2
3	Range and Azimuth	SPFL	76	685	732	80849	60067	3.9
4	Doppler Velocity, Range and Azimuth	SPFL	104	1073	1655	144001	151712	6.6
5	Range and Azimuth	<24,5>	94.6	381	300	24703	21336	2.8
6	Doppler Velocity, Range and Azimuth	<24,5>	120	638	600	35078	44152	3.3
7	Doppler Velocity, Range and Azimuth (2)	<24,5>	149	800	1152	60956	98122	5.3

*Row 7 corresponds to an alternative serial-parallel configuration with 2 MF IPs.

architecture enables on-the-fly configuration of $\Delta\phi$ which allows significant improvement in execution time. As shown in Fig. 14, the increase in $\Delta\phi$ does not affect the RMSE of range and Doppler velocity. As expected, however, there is a marginal degradation of the RMSE for azimuth. On the other hand, the execution time for $\Delta\phi = 2^\circ$ and $\Delta\phi = 4^\circ$ is 1.96 and 3.75 times lower than that of $\Delta\phi = 1^\circ$. Also, the dynamic power consumption for $\Delta\phi = 2^\circ$ and $\Delta\phi = 4^\circ$ is 15% and 20% times lower than that of $\Delta\phi = 1^\circ$.

Next, we consider the on-the-fly configuration of a second parameter - the number of packets. Based on clutter conditions contributing to lower SNR (for example, clutter differs significantly in rural and urban scenarios), the number of packets in a coherent interval may need to be dynamically adjusted. A fewer number of packets (shorter coherent intervals) can significantly reduce the estimation time. We consider the effect of a number of packets on the RMSE of the Doppler velocity estimation for different SNRs. As shown in Fig. 15, the RMSE of the Doppler estimation increases with a fall in SNR. This is most significant for the third target case which has the lowest signal strength (Fig. 15c). Furthermore, the reduction in RMSE is insignificant after a certain number of packets. On the other hand, execution time is reduced by 9, 5, and 2 factors for 10, 20, and 50 packets when compared to 100 packets. Thus, we can reduce the execution time significantly by reducing the number of packets with a slight degradation in the RMSE. Many applications do not need accurate Doppler velocity but need to know whether the target velocity is within a specific range. For such applications, we can tune the number of Doppler elements, D , which controls the resolution of Doppler velocity estimation. As shown in Fig. 16, the maximum error is $0.6m/s$ and $1.8m/s$ when D is 200 and 40, respectively. On the other hand, the execution time is reduced by a factor of 2.5 for $D = 40$. Since MUSIC IP is active once per target compared to MF IP, which is activated once per packet, there are no significant savings in the overall power consumption of RSP due to the reduced number of packets.

VII. CONCLUSIONS AND FUTURE DIRECTIONS

In this work, we present a reconfigurable digital baseband RSP accelerator capable of three-dimensional target tracking along range, azimuth, and elevation. We have proposed novel IPs for hardware implementations of range-azimuth processing through matched filtering and digital beamforming; multiple target detection using CLEAN; and Doppler estimation using MUSIC algorithms on a Zync

MPSoC. We have innovated a low-complexity framework for two-dimensional range-azimuth processing by exploiting the inherent redundancy in the data processing operations. We have benchmarked the functional correctness of our novel hardware IPs with the implementation of the algorithms in DPFL WL and demonstrated very low RMSE (below 1%) for the estimation of range, Doppler and azimuth for multiple target scenarios. Through our studies on range-azimuth processing, we show that word lengths optimized for a 5-bit integer representation of a total word of 24-bits provide resource and dynamic power savings of the order of 40-76%, and 50% respectively. We examine HSCD between PL and PS on the MPSoC and show that memory resource utilization on PL trades off with execution time; with an optimized architecture realized with Fourier-based range-azimuth processing on the PL and MUSIC-based Doppler estimation on PS. This fixed-point architecture results in an overall acceleration of 95 times with respect to a framework where all the algorithms are implemented entirely on the PS and a 120-factor improvement in execution time over the Quad-core processor. Further, the framework is made reconfigurable with respect to the selection of key parameters such as the azimuth precision and the number of packets in the coherent time interval, which make it suitable for operation under different real-world scenarios where varied clutter and target conditions may be encountered.

Some important points to note: First, the hardware IPs of the RSP algorithms have been realized for a co-designed 802.11ad based JRC with Golay based transmit waveforms. However, these IPs can be modified with minimum changes in the architecture for other types of digital coded radar transmit waveforms. Only the pre-computed 1DFFT sequences in **Step.1** of the RSP would have to be modified for this purpose. Further, the reconfigurable nature of the RSP accelerator could be potentially exploited for on-the-fly changes in the radar transmit waveform. Second, the current version of the RSP assumes a fixed threshold for the detection of the targets; while real-world conditions require an adaptive threshold based on a fixed false alarm rate. In our future work, we will implement adaptive threshold selection based on constant false alarm rates on hardware and integrate the IP with this accelerator.

ACKNOWLEDGEMENT

The authors gratefully acknowledge the financial support obtained from the Ministry of Electronics and Information Technology (MEITY) CC&BT grant from the Government of India and the Qualcomm India Innovation Fellowship 2022.

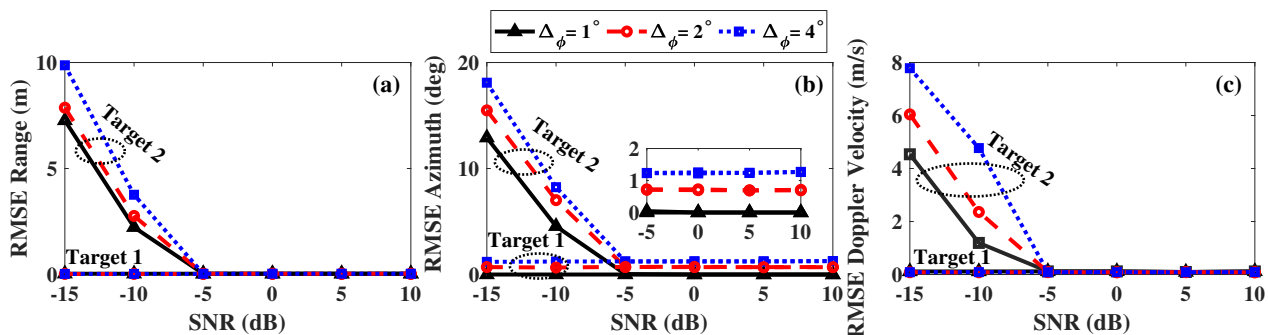


Fig. 14: RMSE for different angular precision values for varying SNR

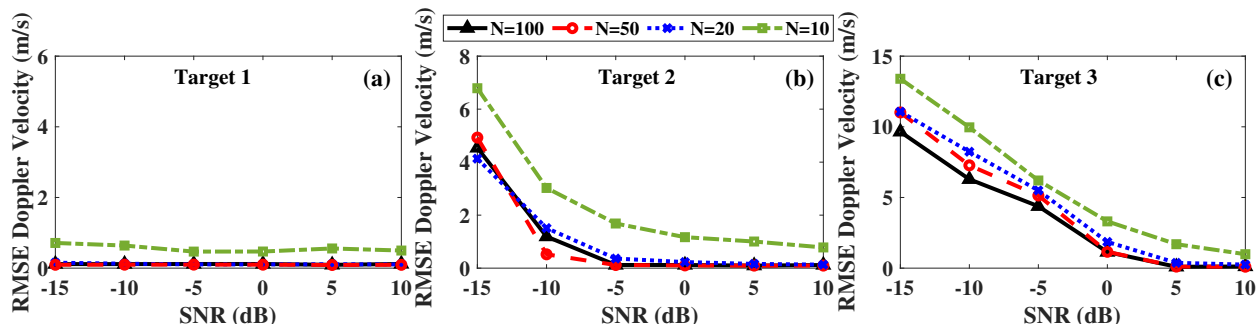


Fig. 15: RMSE for different numbers of packets (coherent processing intervals) for varying SNR

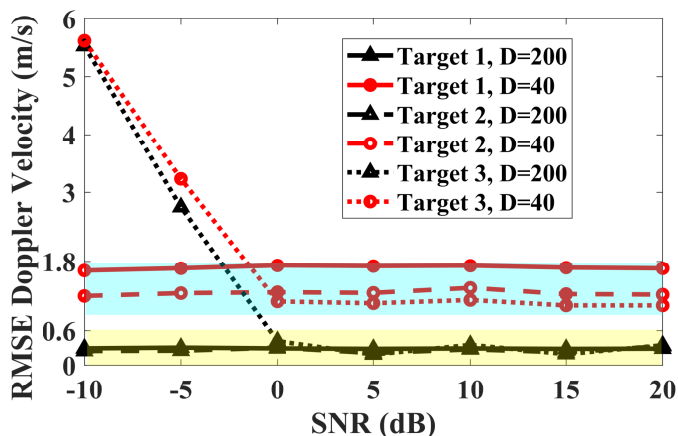


Fig. 16: The effect of the number of Doppler elements, D , on the RMSE of the Doppler velocity for three targets with Doppler velocity spans from -5m/s to 5m/s .

REFERENCES

- [1] B. Li and A. P. Petropulu, "Joint transmit designs for coexistence of MIMO wireless communications and sparse sensing radars in clutter," *IEEE Transactions on Aerospace and Electronic Systems*, vol. 53, no. 6, pp. 2846–2864, 2017.
- [2] A. F. Martone, K. I. Ranney, et al., "Spectrum allocation for noncooperative radar coexistence," *IEEE Transactions on Aerospace and Electronic Systems*, vol. 54, no. 1, pp. 90–105, 2017.
- [3] A. Hassaniien, M. G. Amin, Y. D. Zhang, and F. Ahmad, "Signaling strategies for dual-function radar communications: An overview," *IEEE Aerospace and Electronic Systems Magazine*, vol. 31, no. 10, pp. 36–45, 2016.
- [4] F. Hessar and S. Roy, "Spectrum sharing between a surveillance radar and secondary Wi-Fi networks," *IEEE Transactions on Aerospace and Electronic Systems*, vol. 52, no. 3, pp. 1434–1448, 2016.
- [5] K. V. Mishra, Y. C. Eldar, E. Shoshan, M. Namer, and M. Meltsin, "A cognitive sub-nyquist mimo radar prototype," *IEEE Transactions on Aerospace and Electronic Systems*, vol. 56, no. 2, pp. 937–955, 2019.
- [6] P. Kumari, J. Choi, N. Gonzalez-Prelcic, and R. W. Heath, "IEEE 802.11ad-based radar: An approach to joint vehicular communication-radar system," *IEEE Transactions on Vehicular Technology*, vol. 67, pp. 3012–3027, Apr. 2018.
- [7] G. Duggal, S. Vishwakarma, K. V. Mishra, and S. S. Ram, "Doppler-resilient 802.11 ad-based ultrashort range automotive joint radar-communications system," *IEEE Transactions on Aerospace and Electronic Systems*, vol. 56, no. 5, pp. 4035–4048, 2020.
- [8] A. Hassaniien, M. G. Amin, E. Aboutanios, and B. Himed, "Dual-function radar communication systems: A solution to the spectrum congestion problem," *IEEE Signal Processing Magazine*, vol. 36, no. 5, pp. 115–126, 2019.
- [9] S. S. Ram, S. Singhal, and G. Ghatak, "Optimization of network throughput of joint radar communication system using stochastic geometry," *Frontiers in Signal Processing*, vol. 2, 2022.
- [10] J. B. Kenney, "Dedicated short-range communications (DSRC) standards in the United States," *Proceedings of the IEEE*, vol. 99, no. 7, pp. 1162–1182, 2011.
- [11] A. Asadi, Q. Wang, and V. Mancuso, "A survey on device-to-device communication in cellular networks," *IEEE Communications Surveys & Tutorials*, vol. 16, no. 4, pp. 1801–1819, 2014.
- [12] P. Wang, B. Di, H. Zhang, K. Bian, and L. Song, "Cellular V2X communications in unlicensed spectrum: Harmonious coexistence with VANET in 5G systems," *IEEE Transactions on Wireless Communications*, vol. 17, no. 8, pp. 5212–5224, 2018.
- [13] J. Choi, V. Va, N. Gonzalez-Prelcic, R. Daniels, C. R. Bhat, and R. W. Heath, "Millimeter-wave vehicular communication to support massive automotive sensing," *IEEE Communications Magazine*, vol. 54, no. 12, pp. 160–167, 2016.
- [14] G. Duggal, K. V. Mishra, and S. S. Ram, "Micro-doppler and micro-range detection via doppler-resilient 802.11ad-based vehicle-to-pedestrian radar," in *IEEE Radar Conference 2019*, pp. 1–6, 2019.
- [15] B. Drozdenko, M. Zimmermann, T. Dao, K. Chowdhury, and M. Leeser, "Hardware-software codesign of wireless transceivers on zynq heterogeneous systems," *IEEE Transactions on Emerging Topics in Computing*, vol. 6, no. 4, pp. 566–578, 2017.
- [16] N. Agrawal and S. J. Darak, "Performance analysis of reconfigurable filtered ofdm for Idacs," in *2019 11th International Conference on Communication Systems & Networks (COMSNETS)*, pp. 500–503, IEEE, 2019.
- [17] B. Schweizer, A. Grathwohl, G. Rossi, P. Hinz, C. Knill, S. Stephany, H. J. Ng, and C. Waldschmidt, "The fairy tale of simple all-digital radars: How to deal with 100 gbit/s of a digital millimeter-wave mimo radar on an fpga [application notes]," *IEEE Microwave Magazine*, vol. 22, no. 7, pp. 66–76, 2021.
- [18] G. Zhong, S. Niar, A. Prakash, and T. Mitra, "Design of multiple-target tracking system on heterogeneous system-on-chip devices," *IEEE Transactions on Vehicular Technology*, vol. 65, no. 6, pp. 4802–4812, 2016.

- [19] D. Ma, N. Shlezinger, *et al.*, "Spatial modulation for joint radar-communications systems: Design, analysis, and hardware prototype," *IEEE Transactions on Vehicular Technology*, vol. 70, no. 3, pp. 2283–2298, 2021.
- [20] P. Kumari, A. Mezghani, and R. W. Heath, "JCR70: A low-complexity millimeter-wave proof-of-concept platform for a fully-digital SIMO joint communication-radar," *IEEE Open Journal of Vehicular Technology*, vol. 2, pp. 218–234, 2021.
- [21] J. Pegoraro, J. O. Lacruz, E. Bashirov, M. Rossi, and J. Widmer, "RAPID: Retrofitting IEEE 802.11 ay access points for indoor human detection and sensing," *ArXiv Preprint arXiv:2109.04819*, 2021.
- [22] M. Alae-Kerahroodi, E. Raci, S. Kumar, and B. S. MRR, "Cognitive radar waveform design and prototype for coexistence with communications," *IEEE Sensors Journal*, vol. 22, no. 10, pp. 9787–9802, 2022.
- [23] A. R. Chiriyath, S. Ragi, H. D. Mittelman, and D. W. Bliss, "Novel radar waveform optimization for a cooperative radar-communications system," *IEEE Transactions on Aerospace and Electronic Systems*, vol. 55, no. 3, pp. 1160–1173, 2019.
- [24] S. Zhou, X. Liang, Y. Yu, and H. Liu, "Joint radar-communications co-use waveform design using optimized phase perturbation," *IEEE Transactions on Aerospace and Electronic Systems*, vol. 55, no. 3, pp. 1227–1240, 2019.
- [25] K. V. Mishra, M. B. Shankar, V. Koivunen, B. Ottersten, and S. A. Vorobyov, "Toward millimeter-wave joint radar communications: A signal processing perspective," *IEEE Signal Processing Magazine*, vol. 36, no. 5, pp. 100–114, 2019.
- [26] J. A. Zhang, F. Liu, C. Masouros, R. W. Heath, Z. Feng, L. Zheng, and A. Petropulu, "An overview of signal processing techniques for joint communication and radar sensing," *IEEE Journal of Selected Topics in Signal Processing*, vol. 15, no. 6, pp. 1295–1315, 2021.
- [27] A. Sneh, S. Jain, V. Sindhu, S. S. Ram, and S. Darak, "Ieee 802.11 ad based joint radar communication transceiver: Design, prototype and performance analysis," *arXiv preprint arXiv:2209.04235*, 2022.
- [28] S. Ahmad, V. Boppana, I. Ganusov, V. Kathail, V. Rajagopalan, and R. Wittig, "A 16-nm multiprocessing system-on-chip field-programmable gate array platform," *IEEE Micro*, vol. 36, no. 2, pp. 48–62, 2016.
- [29] "Ac 10 radar." <http://www.trw.com> [TRW,Livonia,MI,USA].
- [30] R. Rajesh, S. J. Darak, A. Jain, S. Chandhok, and A. Sharma, "Hardware–software co-design of statistical and deep-learning frameworks for wideband sensing on zynq system on chip," *IEEE Transactions on Very Large Scale Integration (VLSI) Systems*, vol. 31, no. 1, pp. 79–89, 2023.
- [31] J. Goldsmith, C. Ramsay, D. Northcote, K. W. Barlee, L. H. Crockett, and R. W. Stewart, "Control and visualisation of a software defined radio system on the xilinx rfsoc platform using the pynq framework," *IEEE Access*, vol. 8, pp. 129012–129031, 2020.
- [32] J. Tsao and B. D. Steinberg, "Reduction of sidelobe and speckle artifacts in microwave imaging: The clean technique," *IEEE Transactions on Antennas and Propagation*, vol. 36, no. 4, pp. 543–556, 1988.
- [33] S. S. Ram and H. Ling, "Through-wall tracking of human movers using joint doppler and array processing," *IEEE Geoscience and Remote Sensing Letters*, vol. 5, no. 3, pp. 537–541, 2008.
- [34] R. Schmidt, "Multiple emitter location and signal parameter estimation," *IEEE transactions on antennas and propagation*, vol. 34, no. 3, pp. 276–280, 1986.
- [35] J. G. Francis, "The qr transformation—part 2," *The Computer Journal*, vol. 4, no. 4, pp. 332–345, 1962.
- [36] M. Skolnik, "Introduction to radar systems, third edition," *McGraw-Hil Book*, 2001.